Title

Validation of an MR-based multimodal method for molecular composition and proton stopping power ratio determination using ex vivo animal tissues and tissue-mimicking phantoms.

Permalink

https://escholarship.org/uc/item/1mt5b560

Journal

Physics in Medicine & Biology, 68(17)

Authors

Marants, Raanan

Tattenberg, Sebastian

Scholey, Jessica

et al.

Publication Date

2023-08-28

DOI

10.1088/1361-6560/ace876

Peer reviewed

Validation of an MR-based multimodal method for molecular composition and proton stopping power ratio determination using *ex vivo* animal tissues and tissue-mimicking phantoms

Raanan Marants[1,*], **Sebastian Tattenberg**[2,3], **Jessica Scholey**[4], **Evangelia Kaza**[1], **Xin Miao**[5], **Thomas Benkert**[6], **Olivia Magneson**[1], **Jade Fischer**[1,7], **Luciano Vinas**[1,8], **Katharina Niepel**[2], **Thomas Bortfeld**[3], **Guillaume Landry**[9,10], **Katia Parodi**[2,10], **Joost Verburg**[3], **Atchar Sudhyadhom**[1]

[1.] Department of Radiation Oncology, Dana-Farber Cancer Institute, Brigham and Women's Hospital, and Harvard Medical School, Boston, Massachusetts, United States of America

[2.] Department of Medical Physics, Faculty of Physics, Ludwig-Maximilians-Universität München, Garching, Germany

[3.] Division of Radiation Biophysics, Department of Radiation Oncology, Massachusetts General Hospital and Harvard Medical School, Boston, Massachusetts, United States of America

[4.] Department of Radiation Oncology, University of California, San Francisco, San Francisco, California, United States of America

[5.] Siemens Medical Solutions USA Inc., Boston, Massachusetts, United States of America

[6.] Siemens Healthcare GmbH, Erlangen, Germany

[7.] Department of Medical Physics, University of Calgary, Calgary, Alberta, Canada

[8.] Department of Statistics, University of California, Los Angeles, Los Angeles, California, United States of America

[9.] Department of Radiation Oncology, University Hospital, Ludwig-Maximilians-Universität München, Munich, Germany

[10.] German Cancer Consortium (DKTK), Partner Site Munich, Munich, Germany

Abstract

Objective: Range uncertainty in proton therapy is an important factor limiting clinical effectiveness. Magnetic resonance imaging (MRI) can measure voxel-wise molecular composition and, when combined with kilovoltage CT (kVCT), accurately determine mean ionization potential (I_m), electron density, and stopping power ratio (SPR). We aimed to develop a novel MR-based multimodal method to accurately determine SPR and molecular compositions. This method was evaluated in tissue-mimicking and *ex vivo* porcine phantoms, and in a brain radiotherapy patient.

Approach: Four tissue-mimicking phantoms with known compositions, two porcine tissue phantoms, and a brain cancer patient were imaged with kVCT and MRI. Three imaging-based

*Author to whom any correspondence should be addressed. raanan.marants@rmp.uhn.ca.

values were determined: SPR_{CM} (CT-based Multimodal), SPR_{MM} (MR-based Multimodal), and SPR_{stoich} (stoichiometric calibration). MRI was used to determine two tissue-specific quantities of the Bethe Bloch equation (I_m, electron density) to compute SPR_{CM} and SPR_{MM}. Imaging-based SPRs were compared to measurements for phantoms in a proton beam using a multilayer ionization chamber (SPR_{MLIC}).

Main Results: Root mean square errors relative to SPR_{MLIC} were 0.0104(0.86%), 0.0046(0.45%), and 0.0142(1.31%) for SPR_{CM}, SPR_{MM}, and SPR_{stoich}, respectively. The largest errors were in bony phantoms, while soft tissue and porcine tissue phantoms had <1% errors across all SPR values. Relative to known physical molecular compositions, imaging-determined compositions differed by approximately 10%. In the brain case, the largest differences between SPR_{stoich} and SPR_{MM} were in bone and high lipids/fat tissue. The magnitudes and trends of these differences matched phantom results.

Significance: Our MR-based multimodal method determined molecular compositions and SPR in various tissue-mimicking phantoms with high accuracy, as confirmed with proton beam measurements. This method also revealed significant SPR differences compared to stoichiometric kVCT-only calculation in a clinical case, with the largest differences in bone. These findings support that including MRI in proton therapy treatment planning can improve the accuracy of calculated SPR values and reduce range uncertainties.

Keywords

MRI; proton therapy; stopping power ratio; range uncertainty

---

1. Introduction

Compared to traditional photon-based radiotherapy, proton therapy makes use of the clinically advantageous dose distributions of heavy charged particles that are characterized by a low, flat entrance dose and a high, sharp terminal dose (i.e., Bragg peak) (Levin et al., 2005). Accurately determining the location of the Bragg peak, which enables excellent target coverage with minimal dose deposition distal to the peak, relies on a relative (to water) stopping power ratio (SPR) map that is patient-, tissue-, and voxel-specific. Despite the theoretical potential for improved radiotherapy treatments, it has been challenging to take full advantage of proton therapy (Hu et al., 2018) in the clinical setting, due in part to limitations in the ability to accurately determine where the beam stops. This uncertainty necessitates conservative beam angle choices and the addition of large treatment margins (typically 3.5% of the beam range plus an additional 1–3 mm) which minimize the biophysical benefit of the Bragg peak (Paganetti, 2012). Recent virtual studies for brain proton therapy have shown that even modest range uncertainty improvements to 2% may allow for novel beam angles and superior normal tissue complication probability (NTCP) (Tattenberg et al., 2022a; Tattenberg et al., 2021). Range uncertainty in proton therapy has been cited as one of the most important factors limiting normal tissue dose sparing and tumor dose escalation (Knopf and Lomax, 2013).

Clinically, SPR is most often determined using a stoichiometric calibration of single energy spectrum kilovoltage computed tomography (CT) Hounsfield Unit (HU) (Schaffner and

Pedroni, 1998). However, this approach carries with it considerable sources of uncertainty due to HU-to-SPR degeneracy and deviation of actual human body elemental compositions from ICRU standard tissue (i.e., density changes and elemental composition changes in the mean ionization potential, I_m, that are not patient-specific) (Paganetti, 2012; Yang et al., 2012). Various strategies have been proposed to reduce these errors and mitigate range uncertainty, including dual energy CT (DECT) (Bär et al., 2017; Niepel et al., 2021; Yang et al., 2012), proton CT (Schulte and Penfold, 2012; Dedes et al., 2019), and prompt gamma-ray spectroscopy (Verburg et al., 2013; Tattenberg et al., 2022b), each with its own advantages and limitations. In particular, DECT has been explored by several research groups, where the ability to perform material decomposition can theoretically reduce proton range uncertainty to sub-percent levels (Landry et al., 2011; Hunemohr et al., 2013; Bourque et al., 2014; Hunemohr et al., 2014a; Hunemohr et al., 2014b; Han et al., 2016; Taasti et al., 2016; Peters et al., 2022). DECT applications in proton therapy planning have been clinically implemented though with modest improvements in range uncertainty. Margins >2% are still typically required due to new sources of uncertainties related to increased sensitivity to imaging noise and residual beam hardening effects that are particularly pronounced at lower energies (Li et al., 2017; Bär et al., 2017; Peters et al., 2022).

Magnetic resonance imaging (MRI) has recently grown in prominence as an alternative imaging modality to CT in radiation oncology with many centers now simulating with MRI and, separately, treating with MR-linac machines (Keall et al., 2022; Kurz et al., 2020; Hoffmann et al., 2020). This growing trend of MR in radiotherapy is due in part to MRI offering improved soft tissue contrast and structure visualization compared to CT-based imaging methods (Dirix et al., 2014). In particular, this soft tissue advantage allows for quantification of water, fat, and even hydrogen content which can imply aggregate or average elemental composition (Scholey et al., 2021; Sudhyadhom, 2017). Recently, it has been shown that the primary factors contributing to proton beam range uncertainty, due to translation of imaging data to SPR, may be overcome when using information obtainable by MRI (Scholey et al., 2021; Saito, 2023).

As opposed to stoichiometric calibration, SPR can be directly calculated by the Bethe-Bloch equation if I_m and electron density (ED) values are known. It has previously been shown that MR-based compositional information can provide accurate determinations of I_m using a parameterized model (Unified Compositions, UC) to determine I_m in human biological tissue (Sudhyadhom, 2017). In that study, it was demonstrated that SPR determined with the UC model I_m via a multimodal imaging approach using MRI with CT was in close agreement to SPR calculated from physical measurements for various tissue-mimicking phantoms (Scholey et al., 2021). However, it was found that accurate ED determination required megavoltage CT (MVCT), as kilovoltage CT (kVCT) resulted in significant uncertainties in SPR (Scholey et al., 2021). This result was expected as MVCT has both a stronger linear and one-to-one relationship with ED compared to kVCT, due to MVCT being highly weighted by Compton scattering and relatively independent of atomic number (Langen et al., 2005; Scholey et al., 2021). While useful for highly accurate ED, MVCT imaging has various noise and contrast limitations compared to kVCT and is not readily accessible in most radiation oncology departments owing to it being clinically available only on certain

radiotherapy devices such as TomoTherapy and Radixact machines. To address this, a process was developed to directly determine ED using MR-based knowledge of molecular compositions in combination with kilovoltage CT HU. This process is designated in this manuscript as Molecularly-based Electron Density (MED) (Sudhyadhom, 2020). In the work of Sudhyadhom (Sudhyadhom, 2020), it was shown that MED could be calculated more accurately than by ED determined by kVCT via interpolation of a calibration curve and provided MVCT-level ED accuracy.

In this manuscript, we describe a novel MR-based Multimodal (MM) method to determine SPR and molecular compositions. This MM method, which depends on data from kVCT and MRI, combines two separate MR-based frameworks for calculating mean ionization potential (UC model I_m) and electron density (MED) previously developed by Sudhyadhom. These independent methods are, for the first time, combined in this work to more accurately determine SPR. We validated the accuracy of this methodology in homogeneous tissue-mimicking phantoms (of known molecular and elemental composition) and in *ex vivo* porcine tissue phantoms by comparing against SPR measurements in a clinical proton beam and against SPR as determined by the stoichiometric method. Finally, SPR determined by this MM method was compared with the standard stoichiometric method in a brain radiotherapy patient.

2. Methods

2.1 SPR Calculation Model – I_m and ED

In this manuscript, SPR was determined from imaging using three separate methods: SPR$_{CM}$, SPR$_{MM}$, SPR$_{stoich}$. SPR$_{CM}$ is a kVCT-based multimodal method using kVCT for ED (ED$_{kVCT}$) and the UC model to determine I_m (Sudhyadhom, 2017). SPR$_{MM}$ is an MR-based multimodal method using MR-derived molecular composition and kVCT for ED (MED) and the UC model to determine I_m (Sudhyadhom, 2017, 2020). SPR$_{stoich}$ was determined by interpolating a stoichiometric calibration for the kVCT scanner used in this study (Schaffner and Pedroni, 1998) using the process previously outlined in Scholey et al. (Scholey et al., 2021). For SPR$_{CM}$ and SPR$_{MM}$, they required combined kVCT and MR imaging for SPR calculation. For ED$_{kVCT}$, a Gammex Model 467 (Gammex; Middleton, WI) electron density phantom was scanned by kVCT and used to create an HU-to-ED calibration curve which was interpolated to calculate subsequent ED$_{kVCT}$ values.

The stopping power ratio (SPR) of a charged particle can be calculated by the Bethe Bloch equation:

$$SPR = \rho_{e,water} \frac{\ln\left[2m_e c^2 \beta^2 / I_m\left(1 - \beta^2\right)\right] - \beta^2}{\ln\left[2m_e c^2 \beta^2 / I_{water}\left(1 - \beta^2\right)\right] - \beta^2} \tag{1}$$

where $\rho_{e,water}$ is the electron density normalized to water electron density (also known as ED), m_e is the mass of the electron, c is the speed of light, β is the velocity of the proton normalized to the speed of light, I_m is the mean ionization potential (also known as the average excitation energy) of the medium, and I_{water} is the mean ionization potential of water.

The only quantities that are medium- and tissue-specific are I_m and $\rho_{e,\,water}$, implying that SPR can be accurately determined should these two quantities be known to high accuracy. In this manuscript, we describe the MRI-based multimodal (MM) method to calculating SPR that combines two previously published methods: 1) to calculate I_m using the unified compositions (UC) method (Sudhyadhom, 2017; Scholey et al., 2021) and 2) to calculate ED using a Molecularly-based Electron Density (MED) method (Sudhyadhom, 2020).

The UC model previously proposed by Sudhyadhom (Sudhyadhom, 2017) and further refined in Scholey et al. (Scholey et al., 2021) is a formalism to calculate mean ionization potential, or I_m, from quantities that are obtained from MRI and kVCT. The specific quantities are percentage (by mass) of water and minerals/hydroxyapatite (HA), as well as the total hydrogen content. The I_m value for each voxel value can be calculated using the following set of equations:

$$
\begin{aligned}
&\ln(I_{voxel}) \\
&= \frac{\left(w_{H_2O}\frac{Z_{H_2O}}{A_{H_2O}}\ln(I_{H_2O})\right) + (1-(w_{H_2O}+w_{HA}))\left(\frac{Z_{org}}{A_{org}}\right)(\ln(A) - B\cdot h_{org}) + \left(w_{HA}\frac{Z_{HA}}{A_{HA}}\ln(I_{HA})\right)}{\frac{Z_{total}}{A_{total}}} \\[2mm]
&\qquad h_{org} = \frac{h_{tot} - (h_{HA}\cdot w_{HA} + h_{H_2O}\cdot w_{H_2O})}{1 - (w_{H_2O}+w_{HA})} \\[2mm]
&\qquad \frac{Z_{total}}{A_{total}} = 0.502 h_{tot} + 0.499 \\[2mm]
&\qquad \frac{Z_{org}}{A_{org}} = 0.490 h_{org} + 0.500
\end{aligned}
\tag{2}
$$

where w_i is the fraction of i by mass, Z_i is the atomic number of i, A_i is the atomic mass of i, I_i is the mean ionization potential of i, h_i is the percent hydrogen by mass of i, and i = water (H_2O), organic (org), and mineralized/hydroxyapatite (HA) tissue components. A comprehensive description of how specific imaging data are used to compute each component in equation [2] is available in Scholey et al. (Scholey et al., 2021). In the current work, the constants in the UC model of equation [2] have been updated to implement the elemental I_m values proposed in Bär et al. (Bär et al., 2018) which results in the following changes: $I_{H_2O} = 78.73$ eV, $I_{HA} = 169.44$ eV, A = 92.70 eV, and B = -3.24.

Analogous to the UC model, ED can be reformulated as a function of molecular composition quantities directly measurable by MRI and CT HU, known as MED. The MED method to calculate ED was previously proposed by Sudhyadhom (Sudhyadhom, 2020) and uses the following equations:

$$
\begin{aligned}
\rho_e &= (HU + 1000) \times \frac{1 + w_{lipids}\beta_{lipids} + w_{proteins}\beta_{proteins} + w_{minerals}\beta_{minerals}}{w_{lipids}\alpha_{lipids} + w_{proteins}\alpha_{proteins} + w_{minerals}\alpha_{minerals} + 1000} \\[2mm]
\alpha_i &= 1000 \times \left(\frac{\mu_i}{\rho_i} \times \frac{\rho_{water}}{\mu_{water}} - 1\right) \\[2mm]
\beta_i &= \left(\frac{Z_i}{A_i} \times \frac{A_{water}}{Z_{water}} - 1\right)
\end{aligned}
\tag{3}
$$

where i = lipids/fats, proteins, or minerals/hydroxyapatite, w_i is the fraction of i by mass, μ_i is the mean attenuation coefficient for a given x-ray energy spectrum, ρ_i is the mass density of i, Z_i is the atomic number of i, A_i is the atomic mass of i, and HU is the Hounsfield Unit of a voxel of a CT scan for a given x-ray energy spectrum. The values for β_i are independent of x-ray energy and beam spectrum, and were determined in a prior study (Sudhyadhom, 2020). The values for α_i are dependent on CT x-ray energy and beam spectrum, and should be determined for each CT scanner at each clinically relevant kVp setting. In the original MED work of Sudhyadhom (Sudhyadhom, 2020), it was shown that α_i values could be calculated in a CIRS electron density phantom (Model 062; CIRS, Norfolk, VA). However, as that phantom was made of non-biological molecular compositions, there were no actual biological molecular compounds (water, fat, protein, and bone) used in its creation. Thus, these α_i likely had a higher amount of uncertainty associated with them as the molecular compositions used in that study were assumed to be close to ICRU standard tissue compositions rather than measured or known.

A summary of the multimodal imaging data pipeline for determining the different SPR values presented in this work is given in Figure 1.

2.2.1   Pork Shoulder Phantoms—In this work, α_i values were determined for our specific CT scanner and scan protocol by scanning an *ex vivo* pork shoulder phantom with MRI, kVCT, and MVCT. This phantom was created by placing a plastic-wrapped pork shoulder in a cylindrical container and filling it with water. This pork shoulder was determined to have significant skin, adipose, muscle, and (dense and spongy) bone components. MED was calculated by kVCT using MR-determined molecular compositions. Water and fat/lipid images created from Dixon MR were used to calculate w_{H_2O}, W_{lipids}, and $W_{proteins}$ components.

The α_i values were determined by minimizing the error between MED (using kVCT and MRI) and ED calculated by MVCT. The α_i values used in this work were determined to be −35.2 for lipids/fat, −7.9 for protein, and 458.4 for minerals/HA. The β_i values were previously determined in Sudhyadhom (Sudhyadhom, 2020) as 0.00499 for lipids/fat, −0.0419 for protein, and −0.113 for minerals/HA.

In a separate but analogous pork shoulder phantom, these optimized α_i values were validated by calculating the mean absolute errors (MAE) between MED and MVCT-based ED which were found to be 0.024, 0.021, and 0.046 for adipose, muscle, and bone, respectively. MAE relative to MVCT for MED and kVCT were similar in adipose and muscle but improved in bone with 0.046 and 0.053 for MED and kVCT, respectively.

2.2.2   Tissue-Mimicking and Porcine Tissue Phantoms – Construction Methods and Composition—Homogeneous tissue-mimicking phantoms, partially derived from animal tissues, were created with known elemental and molecular compositions. Knowledge of composition allowed for assessment of the accuracy of imaging-based metrics. Four tissue-mimicking phantoms were created from varying mixtures of water, gelatin from porcine skin (protein), porcine lard (fat), and hydroxyapatite

(mineralized bone), and were meant to represent the different major types of biological tissues of the human body. The elemental composition of gelatin and lard were determined by CHNS(O) combustion analysis at the UC Berkeley Microanalytical Facility. Phantoms containing water and lard included a small amount of detergent/surfactant (SDS) to encourage mixing of fat with water to improve overall homogeneity. Constituents of each mixture were carefully weighed using two high-precision scales: Practum313–1S (Sartorius Biotech, Germany) for loads below 300 g and HK-3200A (Mars Scale Corporation, Canada) for loads above 300 g. The muscle phantom was created by mixing dissolved gelatin in hot water with dissolved SDS in melted lard. The adipose phantom was created by melting lard. The spongiosa bone phantom was created similar to the muscle phantom but includes dissolving hydroxyapatite in the resulting muscle mixture. The cortical bone phantom was created by dissolving hydroxyapatite in hot water. The method to create most of these tissue mimicking phantoms has been previously described in Scholey et al. (Scholey et al., 2021). Tissue-mimicking phantom types and the material compositional recipes are presented below in Table 1.

In addition, two porcine tissue phantoms were created by combining freshly harvested and finely chopped porcine brain or porcine liver tissue with porcine blood such that small air gaps between adjacent pieces of tissue were predominantly filled. In this work, brain or liver tissue was combined with 16% or 19% blood (by mass), respectively (e.g., 16% of the mass of the brain/blood combination was blood). Total water content for these phantoms was determined by precision weighing before and after dehydration. These phantoms represented more realistic mammalian soft tissue compositions for which the results could be most readily applied to *in vivo* human tissues/organs.

Once prepared, phantom mixtures were transferred from beakers (tissue-mimicking phantoms) or bags (porcine tissue phantoms) to custom rectangular prism-shaped polymethyl methacrylate (PMMA) containers (inner dimensions: $20 \times 10 \times 10$ cm^3). Two individual (i.e., one $20 \times 10 \times 10$ cm^3 compartment) containers and two double (i.e., two $20 \times 10 \times 10$ cm^3 compartments separated by a divider) containers were used. Porcine tissue phantoms were refrigerated immediately to maintain freshness, while tissue-mimicking phantoms cooled and solidified at room temperature first prior to being refrigerated to mitigate the development of air pockets. These prism phantoms were imaged within a larger outer plastic container that was filled with a saline (~0.2% NaCl) solution to mimic overall body size and conditions for both MR and CT imaging. A saline solution was used instead of pure water to mitigate potential dielectric effects during MRI. Small modifications were made to the outer containers such that the encased phantom was suspended at approximately the center of the outer container.

2.3 Image Acquisition and Processing – CT and MRI

Three different imaging modalities were used in this study: MVCT, kVCT, and MRI. As shown in prior works, MVCT is highly linear and most accurate for the determination of electron density (Langen et al., 2005). MVCT scans were acquired on an Accuray TomoTherapy (TomoHD; Accuray, Sunnyvale, CA, USA) using the 3.5 MV energy MVCT beam with fine pitch and 1 mm slice thickness reconstruction. MRI and kVCT scans were

acquired on a 3T MRI scanner (MAGNETOM Vida RT Pro Edition, Siemens Healthcare, Erlangen, Germany) and on a CT scanner (SOMATOM Confidence RT Pro, Siemens Healthcare, Erlangen, Germany), respectively. MVCT scans were acquired for two separate pork shoulder phantoms to determine α_i values in one phantom and validate them in the other. MRI and kVCT were acquired for all phantoms and for the exemplar radiotherapy brain cancer patient. A head protocol kVCT was acquired at 120 kVp and reconstructed to 0.5 mm slice thickness. A multi-echo stack-of-spiral ultrashort echo time (UTE) prototype sequence was acquired with flip angle of 1°, TR of 5 ms, and TE of 0.03 ms and 1.35 ms for the in-phase (1st echo) and out-of-phase (2nd echo) images, respectively. Images were acquired with a $2\times2\times2$ mm^3 isotropic resolution in an acquisition time of approximately 2.5 minutes. The 1st echo (TE = 0.03ms) was used as the highly proton density weighted scan for subsequent image processing steps. Two-point Dixon was used to separate water only and fat/lipid MR signal components from the two-echo scan, resulting in a water image and a fat/lipid image. CT imaging data were rigidly registered (optimizing for mutual information) and resampled to the MR data space (to $2\times2\times2$ mm^3 isotropic voxel resolution with cubic spline interpolation) using MIM Software v7.2.7 (MIM; Cleveland, OH, USA).

Imaging data were read into Python and converted into numpy arrays for processing and analysis. First, an N4 bias field correction was applied to the MR images to correct for low spatial frequency intensity non-uniformity due to B1 field heterogeneities (Tustison et al., 2010). Next, a water-only 3D region of interest (ROI) was created and used to obtain MRI water signal normalization values for the UTE, Dixon water, and Dixon fat data, enabling calculation of h_{tot}, w_{H_2O}, and w_{lipids}, respectively. Water ROIs were created from the saline water that surrounded each tissue-mimicking or porcine tissue phantom container, or pork shoulder phantom. In the case of patient scans, water found in the ventricles, in the form of cerebrospinal fluid (CSF), was used to create an internal water ROI. While N4 bias correction accounts for intrascan (spatial) intensity variations, water ROIs were used to normalize scan intensities to the water signal across scans. In addition, w_{HA} was calculated from kVCT-based physical density information using a CT HU to density relationship between density and calcium content derived from previously described bone composition models (Zhou et al., 2009; Scholey et al., 2021) in conjunction with a phantombased mass density calibration. The MR signal in each voxel was assumed to be the sum of water, organic (fat/lipid and proteins), and inorganic (minerals/hydroxyapatite) constituents, and so $W_{proteins}$ was computed as $1 - (w_{H_2O} + w_{lipids} + w_{HA})$. Next, using equations 2 and 3, I_m and MED were computed and used to determine SPR$_{MM}$. The stoichiometric calibration was used to determine SPR$_{stoich}$. Lastly, a cylindrical ROI with diameter ~2.5 cm (to match the diameter of the collecting electrodes of the multi-layer ionization chamber) that extended along the length of the center of each phantom was used to obtain SPR$_{CM}$, SPR$_{MM}$, and SPR$_{stoich}$ values to compare to measured SPR values (see next section). For the human head dataset, SPR values were computed for four tissue types: bone, low density soft tissue, high density soft tissue, and high lipid/fat tissue. The ROI mask for bone was created using a percent by mass hydroxyapatite threshold of $w_{HA} > 12.5$ %. Physical density (PD) thresholds of 0.9<PD<1.0 g/cm^3 and 1.0<PD<1.1 g/cm^3 were used to create ROI masks for low-density

and high-density soft tissue, respectively. The high lipid/fat tissue ROI mask was created by applying threshold of 90% on the w_{lipids} (percent by mass lipid/fat) images.

The patient head MR scan was acquired as part of a prospectively acquired patient imaging study that was approved by the Massachusetts General Brigham Institutional Review Board, protocol #2020P001101, and conducted in accordance with the principles embodied in the Declaration of Helsinki. Informed consent was obtained from the patient.

2.4 Proton Beam Measurements - Phantoms

The method for proton beam measurements was previously reported in Tattenberg et al. (Tattenberg et al., 2022b) and is briefly summarized here. For each phantom, SPR was measured by using a residual range experiment in a Zebra multi-layer ionization chamber (MLIC; IBA Dosimetry, Germany) by irradiating the center of each phantom along its long axis with a 223.6 MeV proton beam (2 nA beam current) that then passed into the collecting electrodes of the MLIC. In addition, MLIC measurements were also performed for an empty air-filled container and a distilled water-filled container. The SPR of each phantom could then be determined with the following equation:

$$SPR_{MLIC} = \left(\frac{R_{phantom}^{80} - R_{air}^{80}}{R_{water}^{80} - R_{air}^{80}} \right)(1 - SPR_{air}) + SPR_{air} \tag{4}$$

where R_i^{80} is the 80% distal fall-off point of the MLIC-measured Bragg peak, i is the phantom, air, or water, and SPR_{air} was based off National Institute of Standards and Technology PSTAR data for a 223.6 MeV proton beam.

3. Results

3.1 Tissue-Mimicking and Porcine Tissue Phantoms SPR and Composition

In this study, SPR was determined by imaging using 3 separate methods: SPR_{CM}, SPR_{MM}, and SPR_{stoich} for the tissue-mimicking and porcine tissue phantoms described in the methods. The accuracy of each of these methods was assessed relative to SPR_{MLIC} determined by proton beam measurements. Table 2 shows a summary of SPR values determined by the various methods with percentage errors (relative to SPR_{MLIC}) calculated and shown in parentheses to the right of the values. Only SPR_{MM} was within 1% of SPR_{MLIC} for all phantoms. Table 3 gives the absolute and relative root mean square errors (RMSE) between SPR_{MLIC} and all other SPR values for different tissue-based phantom groupings. Differences from SPR_{MLIC} were generally greater in bony tissue phantoms compared to soft tissue (including porcine tissue) phantoms. The average RMSEs for all phantoms were 0.0104 (0.86%), 0.0046 (0.45%), and 0.0142 (1.31%) for SPR_{CM}, SPR_{MM}, and SPR_{stoich}, respectively, when compared to SPR_{MLIC}. Imaging-determined percent molecular compositions by mass are shown in Table 4 with subtractive differences/errors relative to known physical molecular composition (from Table 1) shown in parentheses. Generally, subtractive differences/errors in the percent molecular composition are ~10% or less. Water composition tended to be overpredicted in the composite tissue-mimicking phantoms but were closer to physical measurement in the brain and liver porcine tissue phantoms.

3.2 Human Head SPR and Composition

3D maps of SPR_{CM}, SPR_{MM}, and SPR_{stoich} were determined in a radiotherapy brain cancer patient to calculate differences in SPR between the clinical standard stoichiometric method and the two other methods (CM and MM) examined in this study. ROI-averaged SPR values for various tissue types were calculated for these three methods. Results are shown in Table 5 with differences relative to SPR_{stoich} shown in parentheses as ground truth SPR values are not known. The largest differences are in bone and tissues with high lipids/fat, with smaller differences in low- and high-density soft tissue. Overall, SPR_{MM} was in greater disagreement with the SPR_{stoich} compared to SPR_{CM}, where the MAE for all tissue types between SPR_{stoich} and either SPR_{MM} or SPR_{CM} was 1.4% and 0.8%, respectively. This coincides with the results of the previous section, where SPR_{MM} agreed more with SPR_{MLIC} and less with SPR_{stoich} compared to SPR_{CM}. Other than tissues with high lipids/fat, SPR_{stoich} was larger compared with SPR_{CM} and SPR_{MM}. The magnitude of these differences is in line with results seen in the tissue-mimicking phantoms where the largest errors (relative to measured SPR values) were in bone tissues followed by adipose. Exemplar images are shown in Figure 2 with a noticeable anatomic pattern to the SPR differences. Molecular compositions (water, fat/lipid, protein, and minerals) are shown in Figure 3. In general, the ground truth is not known for either SPR or molecular composition. In the special case of CSF, the composition is likely almost entirely water with a density within 0.1% of 1.00 g/cc. In this study, we found the CSF to have an SPR of 0.992, 0.998, and 1.015 for SPR_{CM}, SPR_{MM}, and SPR_{stoich}, respectively, with 94.8% water.

4. Discussion

In this manuscript, we described an MR-based multimodal method, MM, to determine molecular composition, electron density, I_m, and SPR. In contrast to previously published work on a CT-based multimodal method (CM), this MM method integrates MR molecular composition data into the electron density calculation process, which increases the accuracy of electron density calculation and produces more accurate SPR values. This MM method's accuracy was validated with proton beam residual range measurements in tissue-mimicking and *ex vivo* porcine tissue phantoms and found to have an RMSE of 0.0046 (0.45%) and better than 1% SPR accuracy across all tissues studied. This result coincides with the findings of other groups, where Xie et al. (Xie et al., 2018) obtained a RMSE between MLIC-measured SPR and stoichiometric calibration-based SPR in a variety of frozen animal tissues of 0.0250 (1.85%) and 0.0067 (0.62%) for single-energy spectrum CT (SECT) and DECT, respectively, and Taasti et al. (Taasti et al., 2017) found that RMSE (compared to MLIC-measured SPR) decreased from 2.8% to 0.9–1.5% when changing from SECT- to DECT-derived SPR in a large array of animal tissues. In the proton CT studies of Dedes et al. (Dedes et al., 2019) and DeJongh et al. (DeJongh et al., 2021), they independently obtained RMSEs of 0.58% and 0.0039 (0.20%), respectively, between proton CT-based SPR and reference SPR in phantoms with various tissue surrogate inserts. This MM method proved to be more accurate than the clinical standard stoichiometric method, especially in bone tissue. The results of this work are in line with prior groups which have found that the tissue type with largest uncertainty are bone tissues (Niepel et al., 2021; Bär et al.,

2017). The porcine tissues were most accurate which may be due to more realistic molecular compositions, coinciding with what other groups have also found when investigating SPR accuracy by DECT (Niepel et al., 2021; Xie et al., 2018; Taasti et al., 2017).

SPR differences between MM and the stoichiometric method in an example human brain cancer case show a similar pattern of error magnitude to what was seen in the tissue-mimicking phantoms, with the largest differences in bone tissues and high lipids/fat tissues, followed by low- and high-density soft tissues. Similar results were reported by DeJongh et al. (DeJongh et al., 2021), who compared proton CT-derived SPR to x-ray CT-derived SPR in a porcine head phantom. In Table 5, we see that SPR values by stoichiometric method were lower than those of MM and CM for high fat/lipid content tissues, which is consistent with adipose tissue-mimicking phantom results. Interestingly, while high fat/lipid content tissues tend to have lower mass and electron density, SPR values by the stoichiometric method are higher than those of MM and CM for the overall set of low-density soft tissues. These findings imply that the relationship between HU and SPR is, in general, not a one-to-one relationship, but that molecular composition information can improve the accuracy of SPR determination. The stoichiometric calibration assumes specific ICRU compositions for each density, which may not represent actual elemental or molecular compositions for any given individual. In this work, we can directly measure the composition by MRI. In the case of bone, the composition can vary significantly across individuals. Some patients may have bone loss (due to osteoporosis) which may result in lower bone mineral content and greater water content in the pores, for example. It is possible that the assumed ICRU tissue compositions diverge away from this specific individual's composition in bone, an effect that has been shown to result in errors of up to approximately 3.5% (Goma et al., 2018). For high lipid/fat tissues, it may also be the case that the actual composition (high lipid content) differs from the assumed composition used for the stoichiometric calibration, previously shown to yield errors of 2–3% (Jiang et al., 2007). In addition, for this work's high fat tissues, we looked at tissues with >90% lipids which corresponded with ~0.94 SPR$_{stoich}$ (Table 5). Our stoichiometric calibration had 4 distinct regions, with an SPR value of 0.93 being at the inflection point of two regions with very different compositions (lung and fat). In the work of Cui et al. (Cui et al., 2022), they found that SPR$_{stoich}$ errors in adipose tissue were larger (–4.25%) than for other tissue but that these errors could be mitigated in the specific case of breast, where adipose tissue is dominant, by improving the conversion of HU to SPR specifically for adipose tissues.

In general, the ground truth SPR is not known within a patient. In the special case of CSF, the composition is likely almost entirely water with a density within 0.1% of 1.00 g/cc (Lui et al., 1998; Richardson and Wissler, 1996) which implies that the SPR of CSF would be ~1.000. In this study, we found the CSF to have an SPR of 0.992, 0.998, and 1.015 for SPR$_{CM}$, SPR$_{MM}$, and SPR$_{stoich}$, respectively, and close to the expected result for the MM method. Across phantom and patient data, the accuracy of both the CM and MM methods appear to be similar or better than much of the literature on DECT accuracy which has been reported to have a theoretical SPR determination accuracy better than 1% (Hunemohr et al., 2014a; Niepel et al., 2021).

Molecular compositions (i.e., percent mass for water, lipids/fats, proteins, and minerals/hydroxyapatite) determined in this study were in line with the level of accuracy seen in our prior works (Scholey et al., 2021; Sudhyadhom, 2017). Percentage water appeared to have the largest degree of uncertainty (approximately 10%) in tissue-mimicking phantoms and was generally overpredicted. In prior studies, Sudhyadhom evaluated the sensitivity of soft tissue SPR to simulated 10% errors in the percentage water, demonstrating that errors of this magnitude in water content resulted in sub 1% changes in SPR (Sudhyadhom, 2017, 2020). Water composition was more accurate (within ±2%) in porcine tissue phantoms, possibly due to the more realistic nature of the *ex vivo* tissues. Other molecular compositions could not be determined in the porcine tissue phantoms. Fat/lipid composition was slightly more accurate with a combination of over- and under-predicted composition. The accuracy of protein composition was dependent on the accuracy of the other molecular components as $w_{proteins} = 1 - (w_{H_2O} + w_{lipids} + w_{HA})$. Water and fat/lipid composition by MR was determined by a simple 2-point Dixon method which assumes a simple fully in-phase and fully out-of-phase relationship (i.e., single peak) between water and fat/lipid components. In reality, there are multiple lipid peaks, with some partially overlapping the water peak. Additional accuracy in the determination of water, fat/lipid, and protein composition may be possible using a multi-echo multi-peak method (Karampinos et al., 2014). Mineral/hydroxyapatite composition was determined solely by kVCT imaging using a previously derived relationship with mass density (Zhou et al., 2009; Scholey et al., 2021) and may be further improved in the future with additional MR data (Diefenbach et al., 2019; Jerban et al., 2019). In the human head example, compositions were, qualitatively, as would be expected. Regions with CSF (as in the ventricles) were found to have an average of 94.8% water content (Figure 3a; blue arrow) while intraconal tissue surrounding the optic nerves, known as a high fat/lipid area, appeared to have significant fat/lipid content (Figure 3b; red arrow). Based on prior literature, CSF would be expected to be composed of at least 99% water with the remaining 1% being proteins, ions, neurotransmitters, and glucose (Khasawneh et al., 2018; Bulat and Klarica, 2011). Bone appeared to have the most complex composition with spatially varying amounts of mineral and protein content (highest in the cortical bone and lowest in the internal spongiosa bone), adipose/fat content (lowest in the cortical bone and highest in the internal spongiosa bone), and water only in the cortical bone regions. The relative patterns of molecular composition are consistent with those previously reported in the literature (Woodard and White, 1982, 1986; White et al., 1987; White et al., 1991). An additional advantage of the MM and CM methods is that it is possible to also determine mass density from HU and molecular compositions. In the work of Sudhyadhom (Sudhyadhom, 2020), it was shown that mass density can be accurately and directly calculated using a formalism analogous to the one in this work used to calculate MED. Molecular composition may also provide an insight into elemental composition, as average elemental compositions can be assumed for each type of molecule, which along with mass density may be useful in calculating proton dose distributions by Monte Carlo.

CT is the dominant form of imaging used to calculate SPR in large part due to its prevalence in radiation oncology clinics and ease of use. MRI, on the other hand, is not as widely available in radiation oncology as CT simulation but is regularly acquired for diagnostic imaging of many types of patient treatments ranging from intracranial stereotactic

radiosurgery to prostate radiotherapy. In addition, MR simulation is a rapidly growing area of radiation oncology with many centers now acquiring MR scans in addition to CT scans for simulation. MR imaging is also being considered as a potential on-board imaging modality for a future integrated MR-proton machine (Schellhammer et al., 2018a; Schellhammer et al., 2018b; Burigo and Oborn, 2019; Santos et al., 2019; Schellhammer et al., 2019; Hoffmann et al., 2020). In this work, we show that MR data, in conjunction with kVCT imaging, can be used to improve the calculation of SPR by taking advantage of each modality's strengths, specifically MR molecular composition and kVCT density. The MR scans used in this study can be readily added to a diagnostic MR protocol and can be acquired in about 2.5 minutes covering the entire head at a 2mm isotropic resolution. These MR scans could then be registered to a kVCT simulation scan and used to calculate all necessary components as in this work. Such a workflow may allow this MM method to be implemented at most proton therapy centers.

As with all multimodal imaging methods, accurate registration of these images will limit potential clinical implementation accuracy. In this study, we examined phantoms that were immobilized with little to no anatomic deformation. In addition, our *in vivo* imaging study was conducted in the head where rigid registration is known to be highly accurate. Deformable image registration may help to mitigate these errors which might be useful in some body sites with less deformation such as in the pelvis. Future studies will need to be conducted to assess the accuracy in cases with sub-optimal registration before clinical implementation for other body sites can be considered. A potential method to mitigate the error due to registration would be the creation of an MR-only method. Current MR-only methods generally rely on creating a synthetic CT by converting MR images to CT-like data (Wang et al., 2022; Zimmermann et al., 2021; Maspero et al., 2020; Aramburu Nunez et al., 2020; Maspero et al., 2017). While these methods are growing increasingly more realistic and accurate, they generally rely on translating MR intensities to single-energy kVCT HU followed by stoichiometric conversion of synthetic CT HU to SPR. Thus, errors in synthetic CT SPR would combine errors in conversion to CT-like data and stoichiometric SPR errors. Conversion of MR data directly to SPR could be a future direction to increase SPR accuracy and eliminate registration errors that any multimodal method may have.

5. Conclusions

We reported on a novel MR-based multimodal method to determine molecular compositions and SPR. This MM method was validated in tissue-mimicking and *ex vivo* porcine tissue phantoms using proton beam range measurements. We then implemented this method in a brain cancer radiotherapy patient and showed significant differences in SPR calculated by this MM method compared with a stoichiometric kVCT only calculation. The largest differences appeared to be in bone tissues, a tissue type known for higher uncertainty. Additional work will be necessary to validate this method in patients prior to clinical implementation, as inaccurate image registration may lead to higher errors.

Acknowledgements

References

Aramburu Nunez D, Fontenla S, Rydquist L, Del Rosario G, Han Z, Chen CC, Mah D and Tyagi N 2020 Dosimetric evaluation of MR-derived synthetic-CTs for MR-only proton treatment planning Med Dosim 45 264–70 [PubMed: 32089396]

Bär E, Andreo P, Lalonde A, Royle G and Bouchard H 2018 Optimized I-values for use with the Bragg additivity rule and their impact on proton stopping power and range uncertainty Phys Med Biol 63 165007

Bär E, Lalonde A, Royle G, Lu HM and Bouchard H 2017 The potential of dual-energy CT to reduce proton beam range uncertainties Med Phys 44 2332–44 [PubMed: 28295434]

Bourque AE, Carrier JF and Bouchard H 2014 A stoichiometric calibration method for dual energy computed tomography Phys Med Biol 59 2059–88 [PubMed: 24694786]

Bulat M and Klarica M 2011 Recent insights into a new hydrodynamics of the cerebrospinal fluid Brain Res Rev 65 99–112 [PubMed: 20817024]

Burigo LN and Oborn BM 2019 MRI-guided proton therapy planning: accounting for an inline MRI fringe field Phys Med Biol 64 215015

Cui X, Jee K, Hu M, Bao J and Lu HM 2022 Improvement of proton beam range uncertainty in breast treatment using tissue samples Phys Med Biol 67

Dedes G, Dickmann J, Niepel K, Wesp P, Johnson RP, Pankuch M, Bashkirov V, Rit S, Volz L, Schulte RW, Landry G and Parodi K 2019 Experimental comparison of proton CT and dual energy x-ray CT for relative stopping power estimation in proton therapy Phys Med Biol 64 165002

DeJongh DF, DeJongh EA, Rykalin V, DeFillippo G, Pankuch M, Best AW, Coutrakon G, Duffin KL, Karonis NT, Ordonez CE, Sarosiek C, Schulte RW, Winans JR, Block AM, Hentz CL and Welsh JS 2021 A comparison of proton stopping power measured with proton CT and x-ray CT in fresh postmortem porcine structures Med Phys 48 7998–8009 [PubMed: 34739140]

Diefenbach MN, Meineke J, Ruschke S, Baum T, Gersing A and Karampinos DC 2019 On the sensitivity of quantitative susceptibility mapping for measuring trabecular bone density Magn Reson Med 81 1739–54 [PubMed: 30265769]

Dirix P, Haustermans K and Vandecaveye V 2014 The value of magnetic resonance imaging for radiotherapy planning Semin Radiat Oncol 24 151–9 [PubMed: 24931085]

Goma C, Almeida IP and Verhaegen F 2018 Revisiting the single-energy CT calibration for proton therapy treatment planning: a critical look at the stoichiometric method Phys Med Biol 63 235011

Han D, Siebers JV and Williamson JF 2016 A linear, separable two-parameter model for dual energy CT imaging of proton stopping power computation Med Phys 43 600 [PubMed: 26745952]

Hoffmann A, Oborn B, Moteabbed M, Yan S, Bortfeld T, Knopf A, Fuchs H, Georg D, Seco J, Spadea MF, Jakel O, Kurz C and Parodi K 2020 MR-guided proton therapy: a review and a preview Radiat Oncol 15 129 [PubMed: 32471500]

Hu M, Jiang L, Cui X, Zhang J and Yu J 2018 Proton beam therapy for cancer in the era of precision medicine J Hematol Oncol 11 1–16 [PubMed: 29298689]

Hunemohr N, Krauss B, Dinkel J, Gillmann C, Ackermann B, Jakel O and Greilich S 2013 Ion range estimation by using dual energy computed tomography Z Med Phys 23 300–13 [PubMed: 23597413]

Hunemohr N, Krauss B, Tremmel C, Ackermann B, Jakel O and Greilich S 2014a Experimental verification of ion stopping power prediction from dual energy CT data in tissue surrogates Phys Med Biol 59 83–96 [PubMed: 24334601]

Hunemohr N, Paganetti H, Greilich S, Jakel O and Seco J 2014b Tissue decomposition from dual energy CT data for MC based dose calculation in particle therapy Med Phys 41 061714

Jerban S, Lu X, Jang H, Ma Y, Namiranian B, Le N, Li Y, Chang EY and Du J 2019 Significant correlations between human cortical bone mineral density and quantitative susceptibility mapping (QSM) obtained with 3D Cones ultrashort echo time magnetic resonance imaging (UTE-MRI) Magn Reson Imaging 62 104–10 [PubMed: 31247253]

Jiang H, Seco J and Paganetti H 2007 Effects of Hounsfield number conversion on CT based proton Monte Carlo dose calculations Med Phys 34 1439–49 [PubMed: 17500475]

Karampinos DC, Melkus G, Baum T, Bauer JS, Rummeny EJ and Krug R 2014 Bone marrow fat quantification in the presence of trabecular bone: initial comparison between water-fat imaging and single-voxel MRS Magn Reson Med 71 1158–65 [PubMed: 23657998]

Keall PJ, Brighi C, Glide-Hurst C, Liney G, Liu PZY, Lydiard S, Paganelli C, Pham T, Shan S, Tree AC, van der Heide UA, Waddington DEJ and Whelan B 2022 Integrated MRI-guided radiotherapy - opportunities and challenges Nat Rev Clin Oncol 19 458–70 [PubMed: 35440773]

Khasawneh AH, Garling RJ and Harris CA 2018 Cerebrospinal fluid circulation: What do we know and how do we know it? Brain Circ 4 14–8 [PubMed: 30276331]

Knopf AC and Lomax AJ 2013 In vivo proton range verification: a review Phys Med Biol 58 R131–60 [PubMed: 23863203]

Kurz C, Buizza G, Landry G, Kamp F, Rabe M, Paganelli C, Baroni G, Reiner M, Keall PJ, van den Berg CAT and Riboldi M 2020 Medical physics challenges in clinical MR-guided radiotherapy Radiat Oncol 15 93 [PubMed: 32370788]

Landry G, Reniers B, Granton PV, van Rooijen B, Beaulieu L, Wildberger JE and Verhaegen F 2011 Extracting atomic numbers and electron densities from a dual source dual energy CT scanner: experiments and a simulation model Radiother Oncol 100 375–9 [PubMed: 21924780]

Langen KM, Meeks SL, Poole DO, Wagner TH, Willoughby TR, Kupelian PA, Ruchala KJ, Haimerl J and Olivera GH 2005 The use of megavoltage CT (MVCT) images for dose recomputations Phys Med Biol 50 4259–76 [PubMed: 16148392]

Levin WP, Kooy H, Loeffler JS and DeLaney TF 2005 Proton beam therapy Br J Cancer 93 849–54 [PubMed: 16189526]

Li B, Lee HC, Duan X, Shen C, Zhou L, Jia X and Yang M 2017 Comprehensive analysis of proton range uncertainties related to stopping-power-ratio estimation using dual-energy CT imaging Phys Med Biol 62 7056–74 [PubMed: 28678019]

Lui AC, Polis TZ and Cicutti NJ 1998 Densities of cerebrospinal fluid and spinal anaesthetic solutions in surgical patients at body temperature Can J Anaesth 45 297–303 [PubMed: 9597201]

Maspero M, Bentvelzen LG, Savenije MHF, Guerreiro F, Seravalli E, Janssens GO, van den Berg CAT and Philippens MEP 2020 Deep learning-based synthetic CT generation for paediatric brain MR-only photon and proton radiotherapy Radiother Oncol 153 197–204 [PubMed: 32976877]

Maspero M, van den Berg CAT, Landry G, Belka C, Parodi K, Seevinck PR, Raaymakers BW and Kurz C 2017 Feasibility of MR-only proton dose calculations for prostate cancer radiotherapy using a commercial pseudo-CT generation method Phys Med Biol 62 9159–76 [PubMed: 29076458]

Niepel KB, Stanislawski M, Wuerl M, Doerringer F, Pinto M, Dietrich O, Ertl-Wagner B, Lalonde A, Bouchard H, Pappas E, Yohannes I, Hillbrand M, Landry G and Parodi K 2021 Animal tissue-based quantitative comparison of dual-energy CT to SPR conversion methods using high-resolution gel dosimetry Phys Med Biol 66

Paganetti H 2012 Range uncertainties in proton therapy and the role of Monte Carlo simulation Phys Med Biol 57 R99–R117 [PubMed: 22571913]

Peters N, Wohlfahrt P, Hofmann C, Mohler C, Menkel S, Tschiche M, Krause M, Troost EGC, Enghardt W and Richter C 2022 Reduction of clinical safety margins in proton therapy enabled by the clinical implementation of dual-energy CT for direct stopping-power prediction Radiother Oncol 166 71–8 [PubMed: 34774653]

Richardson MG and Wissler RN 1996 Density of lumbar cerebrospinal fluid in pregnant and nonpregnant humans Anesthesiology 85 326–30 [PubMed: 8712448]

Saito M 2023 MRI-based quantification of carbon and oxygen concentrations in human soft tissues for range verification in proton therapy Med Phys

Santos DM, Wachowicz K, Burke B and Fallone BG 2019 Proton beam behavior in a parallel configured MRI-proton therapy hybrid: Effects of time-varying gradient magnetic fields Med Phys 46 822–38 [PubMed: 30488968]

Schaffner B and Pedroni E 1998 The precision of proton range calculations in proton radiotherapy treatment planning: experimental verification of the relation between CT-HU and proton stopping power Phys Med Biol 43 1579–92 [PubMed: 9651027]

Schellhammer S, Enghardt W, Jäkel O, Technische Universität Dresden and Zentrum für Innovationskompetenz OncoRay 2019 Technical Feasibility of MR-Integrated Proton Therapy Beam Deflection and Image Quality. (Dresden pp 1 Online-Ressource

Schellhammer SM, Gantz S, Luhr A, Oborn BM, Bussmann M and Hoffmann AL 2018a Technical Note: Experimental verification of magnetic field-induced beam deflection and Bragg peak displacement for MR-integrated proton therapy Med Phys 45 3429–34 [PubMed: 29763970]

Schellhammer SM, Hoffmann AL, Gantz S, Smeets J, van der Kraaij E, Quets S, Pieck S, Karsch L and Pawelke J 2018b Integrating a low-field open MR scanner with a static proton research beam line: proof of concept Phys Med Biol 63 23LT01

Scholey JE, Chandramohan D, Naren T, Liu W, Larson PEZ and Sudhyadhom A 2021 Technical Note: A methodology for improved accuracy in stopping power estimation using MRI and CT Med Phys 48 342–53 [PubMed: 33107997]

Schulte RW and Penfold SN 2012 Proton CT for improved stopping power determination in proton therapy, invited Trans Am Nucl Soc 106 55–8 [PubMed: 24771877]

Sudhyadhom A 2017 Determination of mean ionization potential using magnetic resonance imaging for the reduction of proton beam range uncertainties: theory and application Phys Med Biol 62 8521–35 [PubMed: 29077570]

Sudhyadhom A 2020 On the molecular relationship between Hounsfield Unit (HU), mass density, and electron density in computed tomography (CT) PLoS One 15 e0244861

Taasti VT, Michalak GJ, Hansen DC, Deisher AJ, Kruse JJ, Krauss B, Muren LP, Petersen JBB and McCollough CH 2017 Validation of proton stopping power ratio estimation based on dual energy CT using fresh tissue samples Phys Med Biol 63 015012

Taasti VT, Petersen JB, Muren LP, Thygesen J and Hansen DC 2016 A robust empirical parametrization of proton stopping power using dual energy CT Med Phys 43 5547 [PubMed: 27782721]

Tattenberg S, Madden TM, Bortfeld T, Parodi K and Verburg J 2022a Range uncertainty reductions in proton therapy may lead to the feasibility of novel beam arrangements which improve organ-at-risk sparing Med Phys 49 4693–704 [PubMed: 35362163]

Tattenberg S, Madden TM, Gorissen BL, Bortfeld T, Parodi K and Verburg J 2021 Proton range uncertainty reduction benefits for skull base tumors in terms of normal tissue complication probability (NTCP) and healthy tissue doses Med Phys 48 5356–66 [PubMed: 34260085]

Tattenberg S, Marants R, Niepel K, Bortfeld T, Sudhyadhom A, Landry G, Parodi K and Verburg J 2022b Validation of prompt gamma-ray spectroscopy for proton range verification in tissue-mimicking and porcine samples Phys Med Biol 67

Tustison NJ, Avants BB, Cook PA, Zheng Y, Egan A, Yushkevich PA and Gee JC 2010 N4ITK: improved N3 bias correction IEEE Trans Med Imaging 29 1310–20 [PubMed: 20378467]

Verburg JM, Riley K, Bortfeld T and Seco J 2013 Energy- and time-resolved detection of prompt gamma-rays for proton range verification Phys Med Biol 58 L37–49 [PubMed: 24077338]

Wang C, Uh J, Patni T, Merchant T, Li Y, Hua CH and Acharya S 2022 Toward MR-only proton therapy planning for pediatric brain tumors: Synthesis of relative proton stopping power images with multiple sequence MRI and development of an online quality assurance tool Med Phys 49 1559–70 [PubMed: 35075670]

White DR, Widdowson EM, Woodard HQ and Dickerson JW 1991 The composition of body tissues (II). Fetus to young adult Br J Radiol 64 149–59 [PubMed: 2004206]

White DR, Woodard HQ and Hammond SM 1987 Average soft-tissue and bone models for use in radiation dosimetry Br J Radiol 60 907–13 [PubMed: 3664185]

Woodard HQ and White DR 1982 Bone models for use in radiotherapy dosimetry Br J Radiol 55 277–82 [PubMed: 7066638]

Woodard HQ and White DR 1986 The composition of body tissues Br J Radiol 59 1209–18 [PubMed: 3801800]

Xie Y, Ainsley C, Yin L, Zou W, McDonough J, Solberg TD, Lin A and Teo BK 2018 Ex vivo validation of a stoichiometric dual energy CT proton stopping power ratio calibration Phys Med Biol 63 055016

Yang M, Zhu XR, Park PC, Titt U, Mohan R, Virshup G, Clayton JE and Dong L 2012 Comprehensive analysis of proton range uncertainties related to patient stopping-power-ratio estimation using the stoichiometric calibration Phys Med Biol 57 4095–115 [PubMed: 22678123]

Zhou H, Keall PJ and Graves EE 2009 A bone composition model for Monte Carlo x-ray transport simulations Med Phys 36 1008–18 [PubMed: 19378761]

Zimmermann L, Buschmann M, Herrmann H, Heilemann G, Kuess P, Goldner G, Nyholm T, Georg D and Nesvacil N 2021 An MR-only acquisition and artificial intelligence based image-processing protocol for photon and proton therapy using a low field MR Z Med Phys 31 78–88 [PubMed: 33455822]
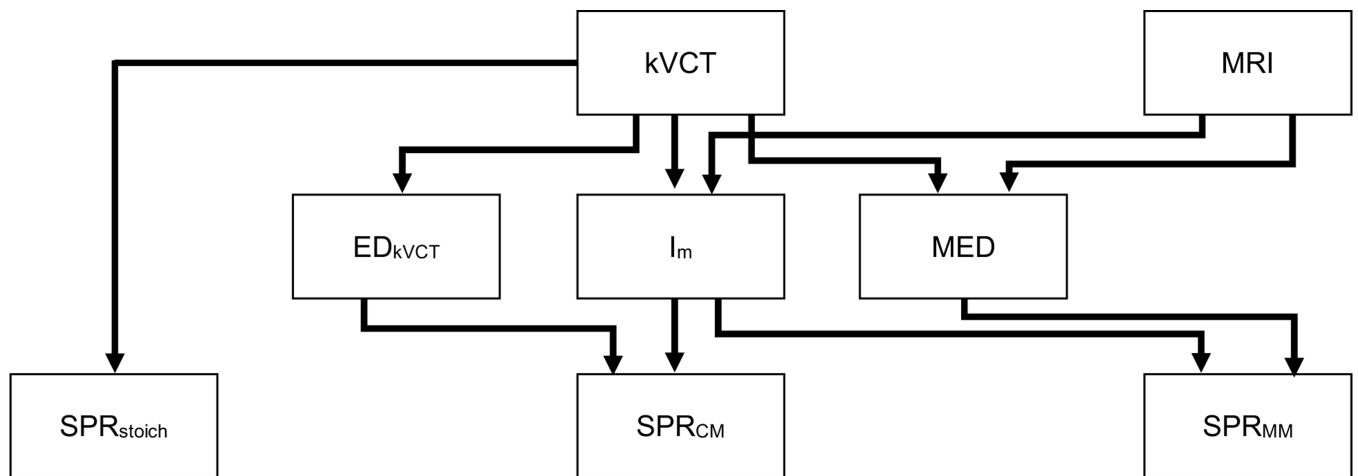
Figure 1.
Multimodal imaging data pipeline for how kVCT and MRI are used to determine the different stopping power ratio (SPR) values presented in this work: SPR_{stoich} (using a stoichiometric calibration), SPR_{CM} (using a CT-based Multimodal method), and SPR_{MM} (an MR-based Multimodal method). SPR values obtained with the Bethe Bloch equation (SPR_{CM} and SPR_{MM}) used a multimodal imaging-based mean ionization potential (I_m) and either a monomodal imaging-based electron density (ED_{kVCT}) or a multimodal imaging-based electron density (MED).
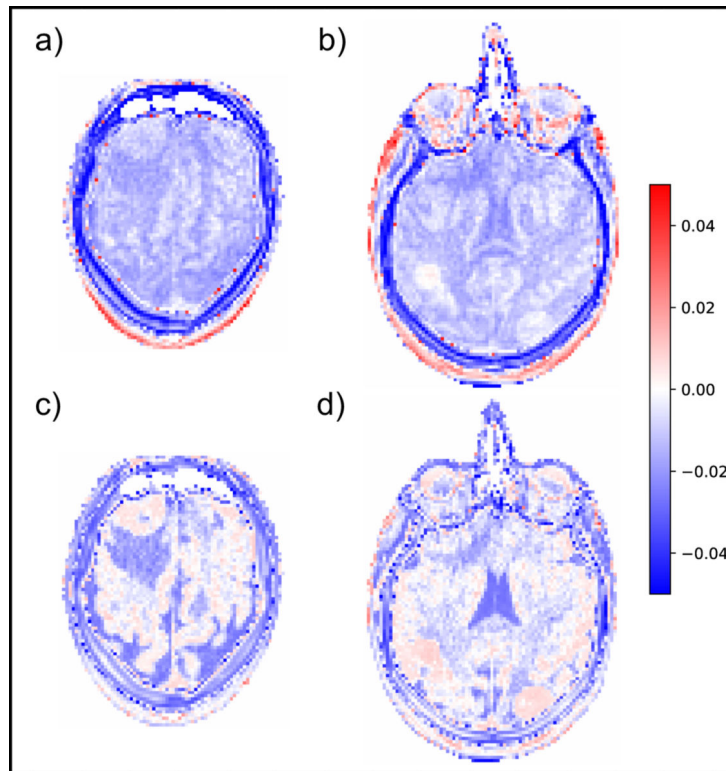
Figure 2.
Exemplar axial SPR difference images for panels a, b: $SPR_{MM} - SPR_{stoich}$ and panels c, d: $SPR_{CM} - SPR_{stoich}$. Difference images show significant amounts of structure due to anatomy- and composition-dependent changes in SPR.
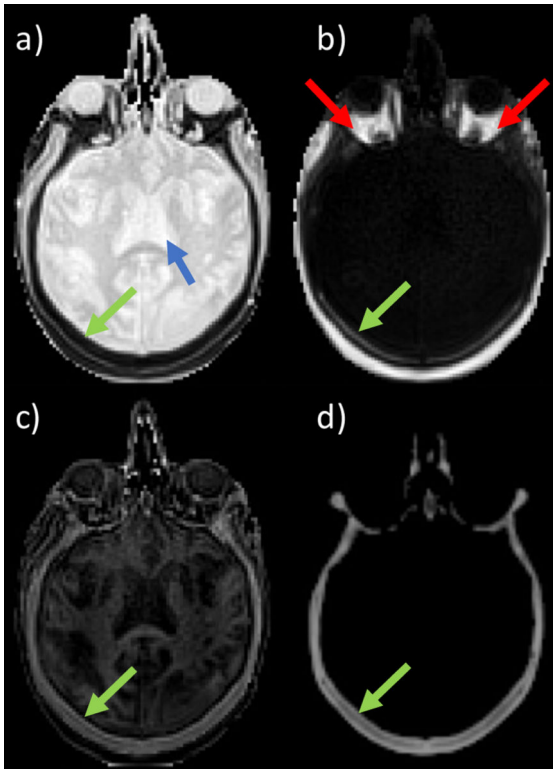
Figure 3.
Exemplar axial slice showing percentage by mass molecular compositions in a human head: a) water, b) lipid/fat, c) protein, and d) minerals/hydroxyapatite. Relative scale with white being 100% and black being 0% for the respective molecule type. Blue arrow represents CSF within the ventricle, red arrow represents intraconal adipose tissue surrounding the optic nerve, and the light green arrow represents bone in the skull.

Table 1.

Physical molecular composition of tissue-mimicking phantom materials as determined by mass percentage during the creation process.

Phantom	Water (%)	Protein (%)	Lipid/Fat (%)	Hydroxyapatite (%)	SDS (%)
Muscle	74.78	19.97	5.00	0.00	0.25
Adipose	0.00	0.00	100.00	0.00	0.00
Spongiosa Bone	26.61	11.83	47.43	12.81	1.32
Cortical Bone	55.00	0.00	0.00	45.00	0.00

Table 2.

SPR values measured by proton beam (MLIC), kVCT-based multimodal (CM), MRI-based multimodal (MM), and stoichiometric method in tissue-mimicking and porcine tissue phantoms. Percentage errors relative to proton beam MLIC data are shown in parentheses.

Phantom	SPR_{MLIC} ($\pm$ 0.005)	SPR_{CM}	SPR_{MM}	SPR_{stoich}
Muscle	1.055	1.056 (0.1%)	1.051 (−0.4%)	1.051 (−0.4%)
Adipose	0.964	0.959 (−0.5%)	0.971 (0.7%)	0.955 (−0.9%)
Spongiosa Bone	1.064	1.079 (1.5%)	1.073 (0.9%)	1.096 (3.1%)
Cortical Bone	1.320	1.345 (1.9%)	1.324 (0.3%)	1.340 (1.5%)
Porcine Brain	1.014	1.019 (0.5%)	1.015 (0.2%)	1.023 (0.9%)
Porcine Liver	1.061	1.059 (−0.2%)	1.059 (−0.2%)	1.062 (0.1%)

Table 3.

Absolute and relative root mean square errors (RMSE) between SPR values measured by proton beam (MLIC) and kVCT-based multimodal (CM), MRI-based multimodal (MM), or stoichiometric method for different tissue-based phantom groupings (bone grouping: spongiosa and cortical, soft tissue grouping: muscle, adipose, porcine brain, and porcine liver).

Phantom Grouping	SPR_{CM} vs. SPR_{MLIC}		SPR_{MM} vs. SPR_{MLIC}		SPR_{stoich} vs. SPR_{MLIC}	
	$RMSE_{abs}$	$RMSE_{rel}$	$RMSE_{abs}$	$RMSE_{rel}$	$RMSE_{abs}$	$RMSE_{rel}$
Bone	0.0144	1.15%	0.0047	0.44%	0.0188	1.73%
Soft Tissue	0.0077	0.67%	0.0046	0.45%	0.0111	1.03%
All	0.0104	0.86%	0.0046	0.45%	0.0142	1.31%

Table 4.

Imaging-based measurement of water, fat/lipid, protein, and mineral/hydroxyapatite (HA) composition in tissue-mimicking and porcine tissue phantoms. Subtractive errors relative to ground truth composition (where appropriate) are shown in parentheses.

Phantom	Water	Lipid/Fat	Protein	Minerals/HA
Muscle	87.1% (12.3)	2.8% (−2.2)	10.2% (−9.8)	0%
Adipose	10.4% (10.4)	91.0% (−9.0)	2.2% (2.2)	0%
Spongiosa Bone	29.5% (2.9)	54.7% (7.3)	5.5% (−6.3)	11.6% (1.2)
Cortical Bone	65.4% (10.4)	7.4% (7.4)	0.3% (0.3)	36.1% (−8.9)
Porcine Brain	85.6% (−1.8)	7.8%	7.9%	0%
Porcine Liver	80.3% (1.1)	6.4%	13.3%	0%

Table 5.

Average SPR values for SPR_{CM}, SPR_{MM}, and SPR_{stoich} across various tissue types in a human head with percentage differences shown in parentheses relative to SPR_{stoich}.

Tissue Type	SPR_{CM}	SPR_{MM}	SPR_{stoich}
Bone	1.403 (−1.2%)	1.391 (−2.1%)	1.420
Low-Density Soft Tissue	0.954 (−0.9%)	0.956 (−0.7%)	0.963
High-Density Soft Tissue	1.023 (−0.6%)	1.020 (−0.9%)	1.029
High Lipids/Fat	0.936 (0.5)	0.948 (1.8)	0.931